Evaluation of Underwater Optical Wireless Channels over $\mathcal{F}$ Turbulence for Different Detection Types

Emna Zedini, *Member, IEEE,* Yalçın Ata, *Senior Member, IEEE,*
Farah Mahdi Al-Sallami, *Member, IEEE,* and Sujan Rajbhandari, *Senior Member, IEEE*

***Abstract*—This paper presents a comprehensive performance study for the underwater optical wireless communication (UOWCs) channel, accounting for the effects of attenuation, turbulence, pointing errors, and fluctuations in the angle-of-arrival (AOA), modeled by the Beer-Lambert model, the Fisher-Snedecor $\mathcal{F}$ turbulence, Hoyt, and Rayleigh distributions, respectively. Considering the stochastic nature of UOWC, closed-form expressions for outage probability, average bit-error-rate (BER), and ergodic capacity are derived. The results revealed that increasing the field-of-view (FoV) reduces the impact of AOA fluctuations. Asymmetric two-dimensional beam misalignment exhibits better outage probability performance compared to symmetric misalignment. Furthermore, heterodyne detection consistently outperforms direct detection. When employing heterodyne detection, M-quadrature amplitude modulation (M-QAM) achieves superior BER performance. Additionally, as absorption increases with longer wavelengths, BER performance deteriorates. Narrower beamwidths improve ergodic capacity by enhancing received signal power.**

***Index Terms*—Underwater wireless optical communication, Turbulence, Absorption, Attenuation, Jerlov water, Angle-of-arrival fluctuations, Pointing error.**

I. Introduction

THE next generation of telecommunication networks demands comprehensive 3-dimensional coverage, encompassing terrestrial, aerial, space, and ocean domains [1]. While the majority of current telecommunication development concentrates on terrestrial applications, it is becoming essential to extend network provision to cover ocean and underwater environments. Underwater communication is crucial for the safety of divers, autonomous underwater vehicles (AUVs) and remote monitoring of the ocean environment. Additionally, the growing presence of underwater infrastructure, including surveying and monitoring activities, underscores the need for robust communication channels between these systems and their control bases [2]. In comparison to terrestrial communications that aim to minimize interference and optimize the allocation of radio resources, underwater optical wireless communication (UOWC) network objectives are to improve transmission capacity, latency, resource sharing, and energy efficiency to enhance the resilience and scalability of underwater services, including communication, sensing, control, computing, and localization [3].

The characteristics of the UOWC medium significantly differ from over-the-air transmission. Due to very high absorption, the radio frequency is unsuitable for UOWC. Despite low absorption and hence wider coverage, acoustic communication offers lower bandwidth (less kHz range), high latency and Doppler spread [4]. This limits its capacity to support underwater applications that demand significantly higher data rates ranging from a few to tens of Mbps [5]. Thus, UOWC has emerged as an alternative to providing high-speed wireless communication [4], [6].

The UOWC channel is very dynamic and offers significant challenges to communication. More specifically, the UOWC is subject to absorption, scattering, beam divergence and strong turbulence [7]–[9]. Because of the highly dynamic environment and various interdependent conditions, modelling the UOWC channel is different and hence, there are several attempts to accurately predict the channel and estimate its capacity. The UOWC depends on various factors such as pointing error, attenuation due to absorption and scattering, and turbulence. Moreover, orientation deviations of the receiver cause changes in the angle-of-arrival (AOA), which in turn leads to fluctuations in the signal-to-noise ratio (SNR) and severely impair the system reliability [10]. The impact of AOA fluctuations-induced fading on UOWC systems has not been well examined in the literature and it has only been studied for FSO systems such as [10] and references therein, where their effect has been modeled using the Rayleigh distribution.

The work in [11] relied on a combination of Monte Carlo simulation and multiple phase screen approaches to produce a simulation-based comprehensive UOWC channel model that considered the impact of absorption, scattering, and turbulence effects. The results revealed that turbulence has a 50% contribution to the the channel impulse response (CIR) peak. Depending upon the strength of the turbulence, various statistical models are adopted for the study of the performance of UOWC such as the Lognormal [12], Generalized Gamma [1], Weibull, and Gamma-Gamma distributions [13], [14] (see [15] for the detailed review on UOWC turbulence and its effect on communication). The work in [16] established a channel model that considered the absorption and multiple

(*Corresponding author: Emna Zedini*)
E. Zedini is with the College of Innovation and Technology, University of Michigan-Flint, Flint, MI, USA (e-mail:ezedini@umich.edu).
Y. Ata is with Department of Electrical and Electronics Engineering, OSTIM Technical University, OSTIM, 06374 Yenimahalle, Ankara, Turkey (e-mail:ylcnata@gmail.com).
F. M. Al-Sallami is with the School of Electronic and Electrical Engineering, University of Leeds, Leeds, UK (e-mails:f.al-sallami@leeds.ac.uk).
S. Rajbhandari is with the Institute of Photonics, University of Strathclyde, Glasgow G1 1RD, UK (e-mails:sujan.rajbhandari@strath.ac.uk).

scattering due to multiple-size bubbles at different positions and densities. The results showed that the power attenuation and scattering increase as the size and density of the bubbles increase. Similarly, the work in [17] modelled the absorption and scattering due to different bubble density, chlorophyll, and suspended particle concentration at different depths of an oblique-range UOWC channel. The study showed that the transmittance varies significantly at different depths and decreases with different trends. Similarly, although the Beer-Lambert law is the most widely used method for estimating attenuation [18], [19], it is not fully accurate for highly scattering media such as UOWC. Several experimental and simulation studies, such as [20]–[24], have demonstrated that the scattering process alters photon propagation directions, causing both temporal and spatial dispersions and hence Beer-Lambert law only offers approximate channel attenuation. The exact nature of these dispersions depends on various factors, such as the field of view (FoV), alignment, and the concentration of scattering particles [20] and overestimate loss in highly scattering media [24]. Furthermore, in addition to the typical noise experienced by communication channels, UOWC channels encounter additional scattering noise introduced by the scattering medium [25] and solar radiation-induced noise in shallow water [21]. The solar radiation-induced noise level depends on factors such as receiver technology, water depth, and transceiver orientation (e.g., a receiver pointed upwards towards the sun experiences higher solar noise levels compared to one pointed towards the horizon).

Several theoretical, simulation and practical investigations aimed to establish the transmission capacity of UOWC. As expected, the data transmission rate depends on various factors such as turbulence strength, modulation schemes and available SNR. Li et al analysed the capacity of optical wireless communication (OWC) links under weak turbulence regimes characterised by Lognormal distribution with pointing error [26]. The study concluded that the scintillation induced by the inner scale has more impact on the capacity than the pointing error variance. Similarly, in [12], a Monte Carlo simulation-based channel capacity estimation was conducted under Log-normal distribution turbulence model. The study concluded that practical modelling of the UOWC channel must combine the effect of turbulence, absorption and scattering. Lognormal distribution was considered to model the oceanic turbulence in [27] along with Rayleigh distributed radial displacement that causes pointing errors and Beer-Lambert path loss. The authors in [28] have analyzed the bit-error-rate (BER) performance of UOWC systems using on-off keying (OOK) modulation and operating under the intensity modulation direct detection (IM/DD) technique. In this analysis, turbulence-induced fading is modeled by the Weibull distribution, while the pointing error effect is characterized by the modified Rayleigh distribution. Similarly, a recent study [29] that investigated the secrecy outage probability (SOP) of UOWC systems considered Weibull distribution to model the salinity-induced ocean turbulence considering its good fit to experimental measurements under practical conditions. In addition to the impact of turbulence, the study considered a modified Rayleigh distribution to model the impact of pointing error, geometry spread and scattering. The results of the study emphasized the dominant effect of scattering on the system. Several studies developed analytical expressions for the ergodic capacity and error performance of UOWC with transmitter or/and receiver spatial diversities [30], [31], [32]. These studies concluded that the diversity scheme can improve channel capacity; however, a careful trade-off is necessary for optimizing performance and complexity.

The previous investigations provided a thorough understanding of the impact of various individual phenomena, and to a limited extent their combined effects, on UOWC performance. However, the literature lacks comprehensive study that combines the impact of adverse channel effects, including turbulence, pointing error, AOA, and attenuation impairments on the performance of UOWC, while accounting for different detection types and making realistic assumptions that reflect practical UOWC channel conditions. Therefore, the contributions of this work are multifold:

- To the best of the authors' knowledge, this is the first study that comprehensively derives the statistics of UOWC channels, considering the combined effects of turbulence, AOA fluctuations, attenuation, and pointing errors, under both heterodyne and IM/DD detection techniques.
- The Hoyt distribution, which allows for distinct deviations in both horizontal and vertical directions, is used to characterize the pointing error.
- The Rayleigh distribution is used to model the AOA fluctuations, and we take into account the impact of FoV variation in our analysis.
- The turbulence-induced fading is assumed to follow the $\mathcal{F}$ distribution that fits experimental data better under all turbulence conditions compared to the Lognormal and Gamma-Gamma models. In addition, its PDF is mathematically simpler, making it attractive from a performance analysis point of view.
- The study derives novel and unified expressions for the fundamental performance metrics of the UOWC system. These measures include the outage probability, ergodic capacity and the average BER for various modulation techniques such as IM/DD OOK and M-ary phase shift keying (M-PSK) as well as M-ary quadrature amplitude modulation (M-QAM) when heterodyne technique is used at the receiver. The obtained results take into account the effects of beam misalignments, aperture diameter, source wavelength, FoV, laser beam waist, and the type of water based on the chlorophyll concentration.
- At high SNR, highly accurate asymptotic results for the outage probability, the average BER, and the ergodic capacity are presented using simple functions.

Similar to other studies on channel capacity [10], [12], [14], [26], [27], [29], certain transceiver device constraints, such as the bandwidth of the laser and photodiode and temporal dispersion, are not included in the analysis. While these parameters are crucial for the practical design of UOWC systems to maximize data rates, the aim of this paper is to provide a theoretical framework for determining the maximum capacity. This analysis can then be used to design practical

systems that achieve the theoretical maximum.

The remainder of the paper is structured as follows. Section II presents the system and channel models. In Section III, we derive the statistics of the UOWC channel under the combination of multiple adverse channel effects. The performance metrics of the UOWC system employing either IM/DD or heterodyne methods are also provided in Section III with the ergodic capacity result obtained in Section IV followed by the asymptotic results at high signal-to-noise-ratio (SNR) in Section V. The numerical and simulation results are then shown in Section V, and the conclusions are given in Section VI.

II. System and Channel Models

A. System Model

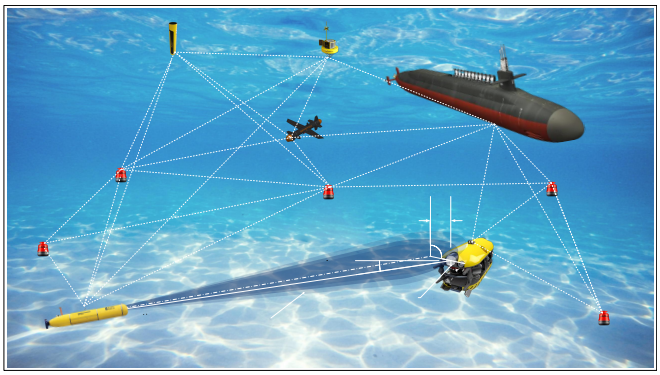

Fig. 1: An UOWC link between an AUV and a remotely operated vehicle (ROV), integral components of the internet of underwater things (IoUT) network. The network also includes other components such as positioning node (PN), transponder, submarine and AUV glider. A solar-powered gateway buoy can collect data.

Fig. 1 illustrates a UOWC link between an AUV and a remotely operated vehicle (ROV), integral components of the internet of underwater things (IoUT) network. The network also includes other components such as positioning node (PNs), transponder, submarine and AUV glider. A solar-powered gateway buoy collects the data. Additionally, this scenario depicts an optical beam transmitted from the AUV to the ROV through the water medium. The beam's transmission is influenced by various factors, including attenuation, turbulence, AOA fluctuations, and pointing errors, which significantly impact the system's performance. Turbulence in the underwater medium induces random fluctuations in the intensity and phase of the optical signal, leading to signal distortion and performance degradation. Additionally, pointing errors caused by misalignment between the transmitter and receiver result in misdirected optical beams and reduced signal strength. To accurately characterize the UOWC channel, a comprehensive model incorporating the effects of the interplay between these factors is vital to evaluate the performance of UOWC systems measured by the BER, outage probability and channel capacity. An insight into the behaviour of the channel devises strategies to mitigate their adverse effects, thereby enhancing the reliability and performance of UOWC systems. The following section investigates the channel model, accounting for the challenging environmental conditions in underwater environments.

B. Channel Model

Assuming that an optical signal propagates through an $\mathcal{F}$ turbulence distributed fading channel along with the effects of attenuation, pointing error and AOA fluctuations, the received signal can be written as

$$y = \eta h\, x + n, \tag{1}$$

where η is the optical-electrical conversion coefficient, x is the transmitted signal, n is the additive white Gaussian noise (AWGN) incorporating the transmitted signal having zero mean and variance $\sigma_n^2 = N_0$, and h is the combined channel state that is defined as

$$h = h_{al} h_{at} h_{pl} h_{af}, \tag{2}$$

where h_{al}, h_{at}, h_{pl} and h_{af} denote the effects of attenuation, turbulence, pointing error and AOA fluctuations, respectively. Depending on the applied detection type, the instantaneous SNR γ can be expressed by [28], [33]

$$\gamma = \frac{(\eta h)^r}{N_0}, \tag{3}$$

where $r = 1$ and $r = 2$ correspond to heterodyne detection and IM/DD schemes, respectively.

1) Attenuation: The underwater medium causes strong attenuation of the optical beam due to absorption and scattering. According to Beer-Lambert law, the attenuation in underwater medium can be expressed by [18], [19]

$$h_{al} = \exp\left[-A(\lambda)L\right], \tag{4}$$

where the attenuation coefficient $A(\lambda)$ is strongly dependent on the wavelength λ and the link length L. The attenuation coefficient $A(\lambda) = a(\lambda) + b(\lambda)$ comprises the absorption $a(\lambda)$ and scattering $b(\lambda)$. Several empirical and theoretical analyzes showed that the blue-green regions of visible light spectrum expose lowest absorption effect comparing with other regions and the chlorophyll concentration is the main determining factor for the attenuation coefficients [18], [19], [34]. The attenuation coefficient due to absorption can be expressed as [18]

$$a(\lambda) = a_w(\lambda) + a_{cl}(\lambda) + a_f(\lambda) + a_h(\lambda), \tag{5}$$

where $a_w(\lambda)$ in $1/m$ is the absorption coefficient of pure water and empirically calculated for different wavelength samples in pure water in [19], $a_{cl}(\lambda) = a_c^0(\lambda)\left(\frac{C_c}{C_c^0}\right)^{0.602}$ denotes the absorption coefficient of the chlorophyll, $a_c^0(\lambda)$ gives the specific absorption coefficient of the chlorophyll, C_c in mg/m^3 is the total concentration of the chlorophyll, $C_c^0 = 1$ mg/m^3 is the chlorophyll concentration, $a_f(\lambda) = a_f^0 C_f \exp(-k_f\lambda)$ represents the absorption coefficient of fulvic acid, $a_f^0 = 35.959\,\mathrm{m}^2/\mathrm{mg}$ is the specific absorption of fulvic acid, $C_f = 1.74098 C_c \exp\left[\frac{0.12327 C_c}{C_c^0}\right]$ reflects the concentration of fulvic acid in mg/m^3, $k_f = \frac{0.0189}{\mathrm{nm}}$, $a_h(\lambda) = a_h^0 C_h \exp(-k_h\lambda)$ is the absorption coefficient of humic acid, $a_h^0 = 18.828\,\mathrm{m}^2/\mathrm{mg}$

represents the specific absorption of humic acid, $C_h = 0.19334 C_c \exp\left[\frac{0.12343 C_c}{C_c^0}\right]$ is the concentration of humic acid in mg/m^3, $k_h = \frac{0.01105}{\text{nm}}$.

The scattering coefficient $b(\lambda)$ in underwater is also defined as [18], [34]

$$b(\lambda) = b_w(\lambda) + b_s^0(\lambda) C_s + b_l^0(\lambda) C_l, \tag{6}$$

where $b_w(\lambda) = 0.005826 \left(\frac{400}{\lambda}\right)^{4.322}$ denotes the scattering coefficient of pure water [19], $b_s^0(\lambda) = 1.151302 \left(\frac{400}{\lambda}\right)^{1.7}$ states the scattering due to small particles, $b_l^0(\lambda) = 0.3411 \left(\frac{400}{\lambda}\right)^{0.3}$ shows the scattering due to large particles, $C_s = 0.01739 C_c \exp\left[\frac{0.11631 C_c}{C_c^0}\right]$ and $C_l = 0.76284 C_c \exp\left[\frac{0.03092 C_c}{C_c^0}\right]$.

2) Turbulence: The $\mathcal{F}$ distribution provides a better fit to experimental data under weak to strong turbulence conditions compared to other models like Lognormal and Gamma-Gamma. Additionally, from a performance analysis perspective, the $\mathcal{F}$ distribution is more appealing because it has a simpler mathematical form in terms of basic elementary functions [35]. Assuming that the UOWC channel is driven by the $\mathcal{F}$ distribution, the probability density function (PDF) of the channel can be written as [35]

$$f_{h_{at}}(h_{at}) = \frac{a^a (b-1)^b h_{at}^{a-1}}{\mathrm{B}(a,b)(a h_{at} + b - 1)^{a+b}}, \quad h_{at} > 0 \tag{7}$$

where $a = \frac{1}{\exp(\sigma_{lnX}^2) - 1}$, $b = \frac{1}{\exp(\sigma_{lnY}^2) - 1}$, and $\mathrm{B}(\cdot,\cdot)$ denotes the Beta function [36, Eq. (8.384/1)]. Here, $\sigma_{\ln X}^2$ and $\sigma_{\ln Y}^2$ represent the log variances indicating the effect of large and small turbulent scales, respectively. Their expressions are provided as follows [37]

$$\sigma_{lnX}^2 = \frac{0.49 \left(\frac{\Omega_G - \Lambda_1}{\Omega_G + \Lambda_1}\right)^2 \sigma_B^2}{\left[1 + \frac{0.4\left(2 - \overline{\Theta}_1\right)\left(\sigma_B/\sigma_R\right)^{12/7}}{\left(\Omega_G + \Lambda_1\right)\left(\frac{1}{3} - \frac{1}{2}\overline{\Theta}_1 + \frac{1}{5}\overline{\Theta}_1^2\right)^{6/7}} + \frac{0.56(1+\Theta_1)}{\sigma_B^{-12/5}}\right]^{7/6}}, \tag{8}$$

$$\sigma_{lnY}^2 = \frac{0.51 \sigma_B^2 \left(1 + 0.69 \sigma_B^{12/5}\right)^{-5/6}}{1 + \left[1.20 \left(\sigma_R/\sigma_B\right)^{12/5} + 0.83 \sigma_R^{12/5}\right] / \left(\Omega_G + \Lambda_1\right)} \tag{9}$$

where $\Omega_G = 2L/kW_G^2$ is the spot radius of the collecting lens, W_G is the radius of the Gaussian lens and $W_G^2 = D_G^2/8$, $\Lambda_1 = \Lambda_0/(\Theta_0^2 + \Lambda_0^2)$ is the Fresnel ratio of Gaussian beam at receiver, $\Lambda_0 = 2L/kW_0^2$, W_0 is the beam radius, $\Theta_0 = 1 - L/F_0$ is the beam curvature parameter at the transmitter, F_0 is the phase front radius of curvature, $\overline{\Theta}_1 = 1 - \Theta_1$ is the complementary parameter, $\Theta_1 = \Theta_0/(\Theta_0^2 + \Lambda_0^2)$ is the beam curvature parameter at receiver. Note that the large- and small-scale turbulence effects, given in (8) and (9), are theoretically derived for atmospheric fluctuations using the Kolmogorov turbulence model. Since these expressions have not yet been validated for UOWC scenarios, and due to the lack of alternative validated models, we adopt these equations for our calculations [33], [38], [39]. In (8) and (9), σ_R^2 and σ_B^2 are the Rytov variances of plane and Gaussian beam waves and they are found in [40] and [41] in analytical form for underwater medium as

$$\sigma_R^2 = \frac{2.9625 k^{7/6} L^{11/6} \beta_0 \left(A^2 \chi_T + B^2 \chi_S + 2AB\chi_{TS}\right)}{\varepsilon^{1/3}}, \tag{10}$$

$$\sigma_B^2 = \frac{20.9845 k^{7/6} L^{11/6} \beta_0 \left(A^2 \chi_T + B^2 \chi_S + 2AB\chi_{TS}\right)}{\varepsilon^{1/3}} \times \mathrm{Re}\left[i^{5/6} \frac{6}{11} {}_2F_1\left(\frac{-5}{6}, \frac{11}{6}; \frac{17}{6}; \left(\overline{\Theta}_1 + \Lambda_1 i\right)\right) - \frac{3}{8}\Lambda_1^{5/6}\right], \tag{11}$$

where the wavenumber $k = 2\pi/\lambda$, $\beta_0 = 0.72$, χ_T is the temperature dissipation rate, $\chi_S = d_r \chi_T / H^2$ is the ensemble-averaged variance for salinity dissipation rate, d_r is the eddy diffusivity ratio and it is defined in [42], H is the temperature-salinity gradient ratio, $\chi_{TS} = 0.5(1 + d_r)\chi_T / H$ is the ensemble-averaged variance for the co-spectrum dissipation rate, ${}_aF_b(.)$ is the hypergeometric function, A and B are the linear coefficients depending on the average temperature $\langle T \rangle$, average salinity concentration $\langle S \rangle$ and ε is the energy dissipation rate. There are various practical parameters used to characterize the Oceanic Turbulence Optical Power Spectrum (OTOPS) model that is utilized for the calculation of Rytov variances of both plane and Gaussian beam waves. The details and formulations for the parameters of underwater medium are presented in [43], [44].

3) Pointing error: One of the models used to describe the pointing error is the Hoyt distribution. Since it permits to observe the asymmetric behaviour (i.e., different beam misalignments in horizontal and vertical directions) of the beam misalignment, we use the Hoyt distribution in this study, which is defined in polar coordinates as [45]

$$f_{r_d,\varphi}(r_d, \varphi) = \frac{r_d}{2\pi q_H \sigma_s^2} \exp\left[-\frac{r_d^2 \xi(\varphi)}{2\sigma_s^2}\right], \tag{12}$$

where r_d is the radial displacement at the receiver detector, $q_H = \sigma_z/\sigma_s$ in (0,1] shows the ratio of horizontal and vertical misalignments, σ_s and σ_z are the beam deviations in orthogonal $s = r_d \cos(\varphi)$, $z = r_d \sin(\varphi)$ directions, and

$$\xi(\varphi) = \left[1 - (1 - q_H^2)\cos^2\varphi\right] / q_H^2. \tag{13}$$

The integral form representation of the pointing error is found in [45] as

$$f_{pl}(h_{pl}) = \frac{\eta_s^2}{2\pi q_H} \int_{-\pi}^{\pi} \frac{h_{pl}^{\eta_s^2 \xi(\varphi) - 1}}{A_0^{\eta_s^2 \xi(\varphi)}} d\varphi, \tag{14}$$

where the related parameters are expressed as $\eta_s = 0.5\omega_e/\sigma_s$, $\omega_e = \omega_b \sqrt{\sqrt{\pi}\mathrm{erf}(\upsilon)/(2\upsilon e^{-\upsilon^2})}$, ω_b is the beamwaist, erf(.) is error function, $\upsilon = \sqrt{\pi r_a^2/2}/\omega_b$, $r_a = D_G/2$ is the receiver aperture radius and $A_0 = \mathrm{erf}^2(\upsilon)$.

4) AOA Fluctuations: According to the Rayleigh distribution, the PDF of the random variable θ_d that denotes the

deviation can be expressed as [10]

$$f_{\theta_d}(\theta_d) = \frac{\theta_d}{\sigma_0^2} \exp\left(-\frac{\theta_d^2}{2\sigma_0^2}\right), \tag{15}$$

where σ_0^2 stands for the variance of θ_d.

III. Probabilistic Analysis

Analytical derivations for the PDF, the cumulative distribution function (CDF), and the moments for the SNR are presented in this section. Furthermore, we obtain exact expressions for the UWOC channel's ergodic capacity, average BER, and outage probability (OP), which are valid for both detection types.

A. PDF of the Channel State

Defining h_{ag} as $h_{ag} = h_{al}h_{at}h_{af}$, then the PDF of h_{ag} conditioned on θ_d can be represented as

$$f_{h_{ag}|\theta_d}(h_{ag}) = \int_{\Delta_x}^{\infty} \frac{1}{h_{al}h_{at}} f_{h_{pl}|\theta_d}\left(\frac{h_{ag}}{h_{al}h_{at}}\right) f_{h_{at}}(h_{at}) dh_{at}, \tag{16}$$

where $\Delta_x = \frac{h_{ag}}{h_{al}A_0\cos\theta_d}$ and the PDF of h_{pl} given the deviation angle θ_d can be deduced from (14) as

$$f_{h_{pl}|\theta_d}(h_{pl}) = \frac{\eta_s^2}{2\pi q_H} \int_{-\pi}^{\pi} \frac{h_{pl}^{\eta_s^2\xi(\varphi)-1}}{(A_0\cos\theta_d)^{\eta_s^2\xi(\varphi)}} d\varphi. \tag{17}$$

Following the procedures detailed in Appendix-A, the PDF of the UOWC channel is found to be

$$f_h(h) = \frac{a\eta_s^2\left[1-\exp\left(-\frac{\theta_{FOV}^2}{2\sigma_0^2}\right)\right]}{2\pi q_H A_0 h_{al}(b-1)\Gamma(a)\Gamma(b)} \times \int_{-\pi}^{\pi} \mathrm{G}_{2,2}^{2,1}\left[\frac{ah}{(b-1)A_0h_{al}}\middle| \begin{matrix} -b, \eta_s^2\xi(\varphi) \\ a-1, \eta_s^2\xi(\varphi)-1 \end{matrix}\right] d\varphi + \exp\left(-\frac{\theta_{FOV}^2}{2\sigma_0^2}\right)\delta(h), \tag{18}$$

where θ_{FOV} refers to the FoV, σ_0 is the standard deviation of the pointing error, $\mathrm{G}_{p,q}^{m,n}(.)$ represents the MeijerG function [36, Eq. (9.301)], and $\delta(.)$ stands for the dirac Delta function.

B. Unified PDF of the SNR

Taking into account various types of detection at the receiver, this section investigates the statistical properties of the electrical SNR of UOWC links using the $\mathcal{F}$ turbulence model under the influence of AOA fluctuations and generalized pointing errors. Specifically, the type of the receiver detection determines how the electrical SNR is calculated as

$$\gamma = \overline{\gamma} h^r, \tag{19}$$

with the IM/DD technique represented by $r = 2$, and the heterodyne technique by $r = 1$, and $\overline{\gamma}$ stands for the average SNR of the UOWC link. In order to prevent fading from either attenuating or amplifying the average transmitted power, we assume that $\mathbb{E}[h] = 1$, where $\mathbb{E}[\cdot]$ denotes the expectation operator. Utilizing (18) and the random variable transformation in (19) along with [36, Eq. (9.31.5)], we derive a unified analytical expression for the SNR PDF of an UOWC link that takes heterodyne and IM/DD detection types into account. This expression is given by

$$f_\gamma(\gamma) = \frac{\eta_s^2\left[1-\exp\left(-\frac{\theta_{FOV}^2}{2\sigma_0^2}\right)\right]}{2\pi q_H r\Gamma(a)\Gamma(b)\gamma} \times \int_{-\pi}^{\pi} \mathrm{G}_{2,2}^{2,1}\left[\frac{a}{(b-1)A_0h_{al}}\left(\frac{\gamma}{\overline{\gamma}}\right)^{\frac{1}{r}}\middle| \begin{matrix} 1-b, 1+\eta_s^2\xi(\varphi) \\ a, \eta_s^2\xi(\varphi) \end{matrix}\right] d\varphi + \frac{1}{r\gamma}\left(\frac{\gamma}{\overline{\gamma}}\right)^{\frac{1}{r}} \delta\left(\left(\frac{\gamma}{\overline{\gamma}}\right)^{\frac{1}{r}}\right) \exp\left(-\frac{\theta_{FOV}^2}{2\sigma_0^2}\right). \tag{20}$$

C. CDF and Moments of the SNR

The CDF of the SNR can be obtained from

$$F_\gamma(\gamma) = \int_0^{\gamma} f_\gamma(t) dt. \tag{21}$$

By following the derivation steps outlined in Appendix-B, we express the CDF of γ as

$$F_\gamma(\gamma) = \frac{\eta_s^2\left[1-\exp\left(-\frac{\theta_{FOV}^2}{2\sigma_0^2}\right)\right]}{2\pi q_H\Gamma(a)\Gamma(b)} \times \int_{-\pi}^{\pi} \mathrm{G}_{3,3}^{2,2}\left[\frac{a}{(b-1)A_0h_{al}}\left(\frac{\gamma}{\overline{\gamma}}\right)^{\frac{1}{r}}\middle| \begin{matrix} 1, 1-b, 1+\eta_s^2\xi(\varphi) \\ a, \eta_s^2\xi(\varphi), 0 \end{matrix}\right] d\varphi + \exp\left(-\frac{\theta_{FOV}^2}{2\sigma_0^2}\right) \mathrm{U}\left(\left(\frac{\gamma}{\overline{\gamma}}\right)^{\frac{1}{r}}\right), \tag{22}$$

where $\mathrm{U}(\cdot)$ denotes the Heaviside step function.

Moreover, the n-th moments of γ for both types of detection techniques can be obtained in exact closed-form as demonstrated in Appendix-C as follows

$$\mathbb{E}[\gamma^n] = \frac{\eta_s^2\,\Gamma(a+rn)\Gamma(b-rn)\left(1-\exp\left(-\frac{\theta_{FOV}^2}{2\sigma_0^2}\right)\right)}{q_H\Gamma(a)\Gamma(b)\sqrt{\left(\frac{\eta_s^2}{q_H^2}+rn\right)(\eta_s^2+rn)}} \times \left[\frac{(b-1)A_0h_{al}}{a}\right]^{rn} \overline{\gamma}^n. \tag{23}$$

Notably, as the subsequent section will show, this formula is very useful in getting asymptotic results for the ergodic capacity at high SNR range.

IV. Exact Analysis

A. Outage Probability Analysis

By utilizing the definition of the OP as $P_{\text{out}} = P_r(\gamma \le \gamma_{\text{th}}) = F_\gamma(\gamma_{\text{th}})$, where γ_{th} represents the threshold SNR, the

expression for the OP develops as

$$P_{\text{out}} = \frac{\eta_s^2 \left[1 - \exp\left(-\frac{\theta_{FOV}^2}{2\sigma_0^2}\right)\right]}{2\pi q_H \Gamma(a)\Gamma(b)} \times \int_{-\pi}^{\pi} \mathrm{G}_{3,3}^{2,2}\left[\frac{a}{(b-1)A_0 h_{al}}\left(\frac{\gamma_{\text{th}}}{\overline{\gamma}}\right)^{\frac{1}{r}} \middle| \begin{matrix} 1, 1-b, 1+\eta_s^2\xi(\varphi) \\ a, \eta_s^2\xi(\varphi), 0 \end{matrix}\right] d\varphi + \exp\left(-\frac{\theta_{FOV}^2}{2\sigma_0^2}\right). \quad (24)$$

B. Average BER Analysis

A unified expression for the average BER that encompasses various modulation schemes can be formulated as [14]

$$P_e = \frac{\delta}{2\Gamma(p)} \sum_{k=1}^{n_x} \int_0^{\infty} \Gamma(p, q_k\gamma) f_\gamma(\gamma) d\gamma, \quad (25)$$

where all related parameters for different types of detection and modulation schemes are listed in Table I. By employing the derivations provided in Appendix-D, we derive the unified average BER for UOWC channels as shown by (26), where $\Delta(k,u) = \frac{u}{k}, \frac{u+1}{k}, \ldots, \frac{u+k-1}{k}$.

C. Ergodic Capacity Analysis

According to [46], the ergodic capacity can be expressed as

$$\overline{C} \triangleq \mathbb{E}\left[\ln\left(1 + c_r\gamma\right)\right] = \int_0^{\infty} \ln(1 + c_r\gamma) f_\gamma(\gamma) d\gamma, \quad (27)$$

where c_r is the constant having the values of $c_1 = 1$ and $c_2 = e/(2\pi)$ for heterodyne (i.e. $r = 1$) and IM/DD (i.e. $r = 2$) schemes, respectively. In line with the derivations provided in Appendix-E, we can derive a unified expression for the ergodic capacity as represented by (28).

V. High SNR Analysis

In this section, we present asymptotic expressions for key performance metrics of the UWOC link, including the OP, the average BER, and the ergodic capacity in the high SNR range, represented by simple functions. These expressions accurately converge to the exact results in the high SNR regime and are particularly valuable for determining the diversity order of the system.

A. Outage Probability

Using analysis given in [47] to replace the MeijerG function in (24) with its equivalent FoxH function and applying [48, Eq. (1.8.4)] with some simplifications, the asymptotic expression of the OP in (24) can be derived at high SNR values as

$$P_{\text{out}} \underset{\overline{\gamma}\gg 1}{\approx} \frac{\eta_s^2 \left[1 - \exp\left(-\frac{\theta_{FOV}^2}{2\sigma_0^2}\right)\right]}{2\pi q_H \Gamma(a)\Gamma(b)} \int_{-\pi}^{\pi} \sum_{j=1}^{2} \Upsilon_j \left(\frac{\gamma_{\text{th}}}{\overline{\gamma}}\right)^{\theta_j} d\varphi + \exp\left(-\frac{\theta_{FOV}^2}{2\sigma_0^2}\right), \quad (29)$$

where

$$\Upsilon_1 = \frac{\Gamma(a+b)}{a(\eta_s^2\xi(\varphi) - a)} \left(\frac{a}{(b-1)A_0 h_{al}}\right)^a, \quad (30)$$

$$\Upsilon_2 = \frac{\Gamma(a - \eta_s^2\xi(\varphi))\Gamma(b + \eta_s^2\xi(\varphi))}{\eta_s^2\xi(\varphi)} \left(\frac{a}{(b-1)A_0 h_{al}}\right)^{\eta_s^2\xi(\varphi)}, \quad (31)$$

TABLE I: Average BER Parameters for Different Modulation Schemes

Modulation Scheme	Detection Type	δ	p	q_k	n_x
BPSK	Heterodyne	1	1/2	1	1
M-PSK		$\frac{2}{\max(\log_2 M, 2)}$	1/2	$\sin^2\left(\frac{(2m-1)\pi}{M}\right)\log_2 M$	$\max\left(\frac{M}{4}, 1\right)$
M-QAM		$\frac{4}{\log_2 M}\left(1 - \frac{1}{\sqrt{M}}\right)$	1/2	$\frac{3(2m-1)^2}{2(M-1)}\log_2 M$	$\frac{\sqrt{M}}{2}$
OOK	IM/DD	1	1/2	1/2	1

$$P_e = \frac{\eta_s^2 r^{a+b-2}\left[1 - \exp\left(-\frac{\theta_{FOV}^2}{2\sigma_0^2}\right)\right]}{(2\pi)^r q_H \Gamma(a)\Gamma(b)} \times \sum_{k=1}^{n_x} \int_{-\pi}^{\pi} \mathrm{G}_{2r+2,2r+1}^{2r,r+2}\left[\left(\frac{a}{(b-1)A_0 h_{al}\left(q_k\overline{\gamma}\right)^{\frac{1}{r}}}\right)^r \middle| \begin{matrix} \Delta(r, 1-b), 1, 1-p, \Delta(r, 1+\eta_s^2\xi(\varphi)) \\ \Delta(r,a), \Delta\left(r, \eta_s^2\xi(\varphi)\right), 0 \end{matrix}\right] d\varphi + \frac{n_x\delta}{2}\exp\left(-\frac{\theta_{FOV}^2}{2\sigma_0^2}\right). \quad (26)$$

$$\overline{C} = \frac{\eta_s^2 r^{a+b-2}\left[1 - \exp\left(-\frac{\theta_{FOV}^2}{2\sigma_0^2}\right)\right]}{(2\pi)^r q_H \Gamma(a)\Gamma(b)} \int_{-\pi}^{\pi} \mathrm{G}_{2r+2,2r+2}^{2r+2,r+1}\left[\left(\frac{a}{(b-1)A_0 h_{al}\left(c_r\overline{\gamma}\right)^{\frac{1}{r}}}\right)^r \middle| \begin{matrix} \Delta(r, 1-b), 0, 1, \Delta(r, 1+\eta_s^2\xi(\varphi)) \\ \Delta(r,a), \Delta\left(r, \eta_s^2\xi(\varphi)\right), 0, 0 \end{matrix}\right] d\varphi. \quad (28)$$

$$\theta_j = \left\{ \frac{a}{r}, \frac{\eta_s^2 \xi(\varphi)}{r} \right\}. \tag{32}$$

It is worth noting that the asymptotic expression of the OP presented in (29) involves only the summation of basic elementary functions, unlike the exact OP expression formulated using the MeijerG function in (24). This simplified result is significantly more analytically tractable, offering high accuracy and perfect convergence to the exact result at high SNR range. Furthermore, exploiting this simplified expression enables the straightforward derivation of the diversity order for the UOWC system as follows

$$\mathcal{G}_d = \min\left(\frac{a}{r}, \frac{\eta_s^2 \xi(\varphi)}{r} \right). \tag{33}$$

B. Average BER

By employing integration by parts, the expression for the average BER in (25) can be rearranged and formulated in terms of the CDF of γ as

$$P_e = \frac{\delta q_k^p}{2\Gamma(p)} \sum_{k=1}^{n_x} \int_0^\infty \gamma^{p-1} e^{-q_k \gamma} F_\gamma(\gamma) d\gamma. \tag{34}$$

Now, in the high SNR domain, a simpler mathematical expression for the average BER may be obtained, which is consistent with the asymptotic analysis of the outage probability. This is accomplished by substituting the high SNR OP expression obtained from (29) into (34), applying [36, Eq. (3.326/2)], and employing the variable transformation $t = (\gamma/\overline{\gamma})^{\frac{1}{r}}$ as outlined below

$$P_e \underset{\overline{\gamma} \gg 1}{\approx} \frac{\delta \eta_s^2 \left[1 - \exp\left(-\frac{\theta_{FOV}^2}{2\sigma_0^2} \right) \right]}{4\pi q_H \Gamma(a)\Gamma(b)\Gamma(p)} \int_{-\pi}^{\pi} \sum_{j=1}^{2} \Upsilon_j \frac{\Gamma(p+\theta_j)}{(q_k \overline{\gamma})^{\theta_j}} d\varphi + \frac{n_x \delta}{2} \exp\left(-\frac{\theta_{FOV}^2}{2\sigma_0^2} \right). \tag{35}$$

C. Ergodic Capacity

Asymptotically, at high average SNR, the ergodic capacity in (28) can be approximated using the first derivative of the moments of γ as [49]

$$\overline{C} \underset{\overline{\gamma} \gg 1}{\approx} \ln(c_r) + \left. \frac{\partial \mathbb{E}[\gamma^n]}{\partial n} \right|_{n=0}. \tag{36}$$

Therefore, at high SNR range, we can obtain an accurate asymptotic result of the ergodic capacity by inserting (23) into (36) and performing a few algebraic manipulations as follows

$$\overline{C} \underset{\overline{\gamma} \gg 1}{\approx} \ln(c_r) + r \left(1 - \exp\left(-\frac{\theta_{FOV}^2}{2\sigma_0^2} \right) \right) \times \left(\psi(a) - \psi(b) + \ln\left(\frac{(b-1) A_0 h_{al} \overline{\gamma}^{\frac{1}{r}}}{a} \right) - \frac{(1+q_H^2)}{2\eta_s^2} \right), \tag{37}$$

where $\psi(\cdot)$ denotes the Digamma (psi) function [36, Eq. (8.360.1)].

VI. Results and Discussion

Using the parameters indicated in Table I, this section examines how the key channel and system parameters affect the performance of the UOWC system, in the presence of turbulence, attenuation, AOA fluctuations, and pointing errors. In addition, computer-based Monte Carlo simulations are presented and compared with the obtained analytical outcomes. The accuracy of the proposed framework is confirmed since there is an excellent match between all of the derived and corresponding Monte Carlo Matlab simulated results over 10^7 realizations.

TABLE I: SYSTEM PARAMETERS

Parameter	Value	Parameter	Value
λ	532 nm	$< \mathrm{T} >$	15 °C
$< \mathrm{S} >$	20 ppt	C_c	0.03 g/m^3
χ_T	10^{-7} K^2/s	ε	10^{-4} m^2/s^3
H	-2 °.ppt^{-1}	σ_s	$1 \times r_a$
L	20 m	q_H	0.7
F_0	∞	D_G, W_0	2 cm, 2 cm
γ_{th}	0 dB	w_b	$7 \times r_a$
σ_0	12 mrad	θ_{FOV}	50 mrad

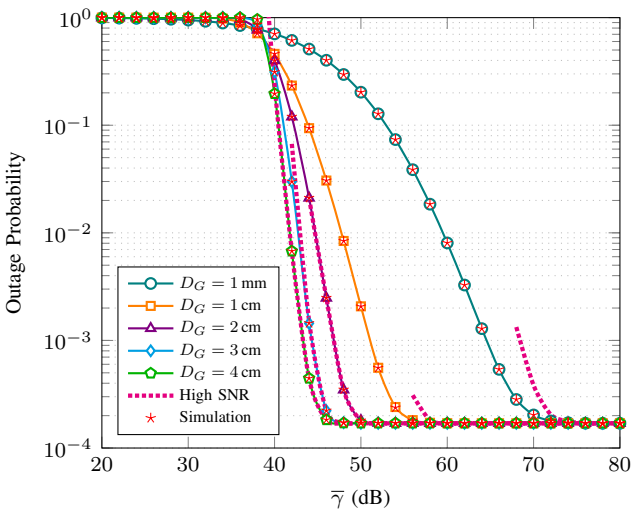

Fig. 2: Outage probability using IM/DD detection for various values of the receiver aperture diameter D_G.

Fig. 2 depicts the outage probability performance when the IM/DD technique is used at the receiver for different values of the receiver aperture diameter D_G. The high SNR asymptotic results are also included, and we can clearly see that they coincide with the exact results at high SNR values, indicating their precision and accuracy. It can also be observed from this figure that the outage probability improves with an increase in the receiver aperture diameter, as expected. An enhancement in the outage probability is also observed with an increase of the average SNR $\overline{\gamma}$ up to 70 dB for all values of D_G. But when $\overline{\gamma}$ exceeds 70 dB, the effect of the AOA fluctuations becomes more pronounced and the outage probability does not improve

even if the average SNR continues to increase. As clearly seen from the figure, an outage probability floor is created as $\overline{\gamma}$ gets larger regardless of the value of D_G.

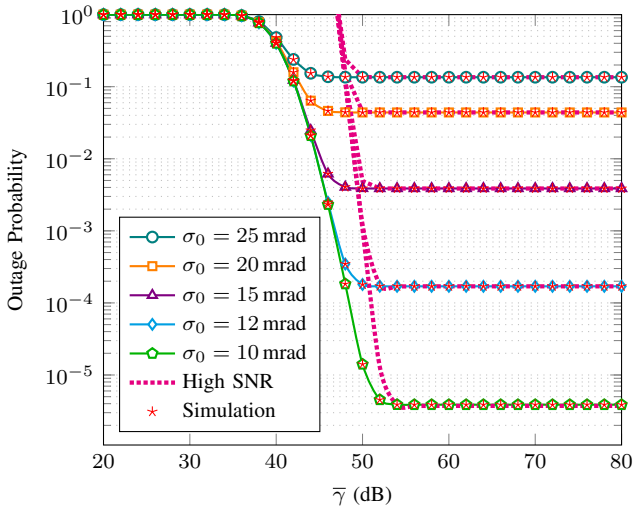

Fig. 3: Outage probability using IM/DD for various values of the beam deviations σ_0.

Fig. 3 illustrates the effect of changing the random orientation deviation levels caused by AOA variations on the outage performance. As this figure shows, the performance of the UOWC link is evidently dependent on variations in the AOA. More precisely, it is notable that an increase in the value of σ_0 corresponds to a higher outage probability, consequently diminishing the performance of the UOWC link. Moreover, we see here the same floor effect, with its level becoming more noticeable as σ_0 increases. Furthermore, it is evident that the asymptotic expression of the outage probability, derived in (29), perfectly converges to the exact result in the high SNR domain, proving the tightness of this asymptotic approximation.

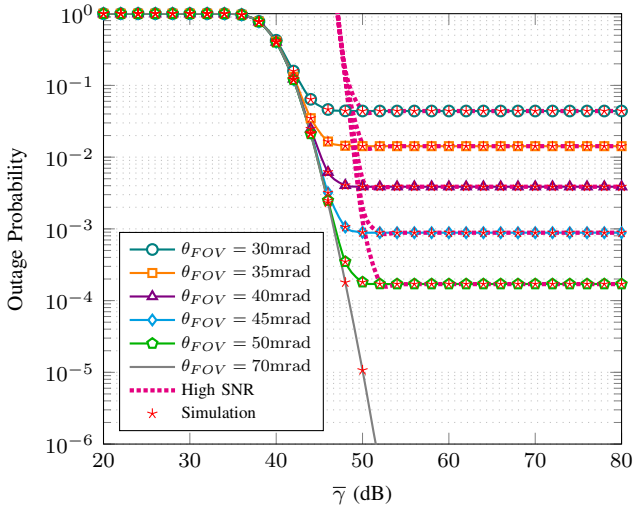

Fig. 4: Outage probability using IM/DD for different values of the receiver FoV.

The effect of the receiver FoV on the outage performance under the IM/DD technique is shown in Fig. 4. We can clearly see that the outage probability improves and the AOA effects become less severe for increasing values of θ_{FOV}. The floor effect is shown here as well and it is evident that its impact decreases significantly with increasing θ_{FOV} values. For instance, the outage floor almost vanishes when a value of $\theta_{FOV} = 70$ mrad is employed. This can be explained by the fact that higher θ_{FOV} values are related to wider receiver field-of-view (FoV), which in turn leads to less impairments from AOA variations. However, optimization is needed because increasing the FoV settings will also increase the background noise effect. Other results that are similar to the previous figures can also be observed from Fig. 4, especially for the high accuracy of the asymptotic expression of the outage probability in the high SNR regime.

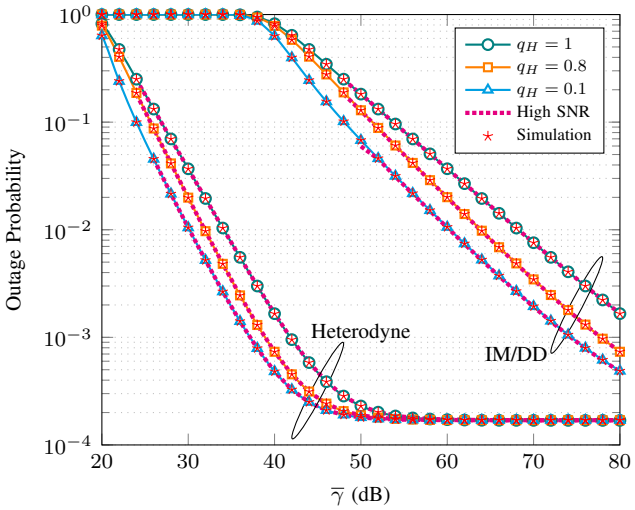

Fig. 5: Outage probability using IM/DD and heterodyne for different ratios of vertical and horizontal beam deviations with $\sigma_s = 3 \times r_a$.

In Fig. 5, the outage probability of the UOWC link using both heterodyne and IM/DD schemes is plotted, for various q_H values with $\sigma_s = 3 \times r_a$. It can be inferred from Fig. 5 that when the beam orientation deviation exhibits asymmetrical behavior, the UOWC communication system performs better regardless of the detection method used at the receiver. For instance, when horizontal and vertical orientation deviations are equal ($q_H = 1$), the outage probability for an average SNR $\overline{\gamma} = 50$ dB is $P_{out} = 1.8210^{-1}$, but when the ratio of horizontal to vertical beam deviations becomes $q_H = 0.1$, the outage probability drops to $P_{out} = 6.79 \times 10^{-2}$ for IM/DD scheme. While heterodyne detection has gained popularity due to its greater sensitivity and ability to better mitigate turbulence effects, compared to the IM/DD technique, it is more complex to implement coherent receivers. Most UOWC systems rely on the direct detection technique because of its simplicity, ease of deployment, and greater robustness to synchronization errors [50].

The average BER using IM/DD OOK modulation scheme for different Jerlov water types is presented in Fig. 6. Depending on the concentration of chlorophyll, different types of water have been classified as pure water, water type I, water type IA, water type IB, and water type II, with the values of the chlorophyll concentration being $C_c = 0.005\,\text{mg/m}^3$,

$C_c = 0.03\,\text{mg/m}^3$, $C_c = 0.1\,\text{mg/m}^3$, $C_c = 0.4\,\text{mg/m}^3$, and $C_c = 1.25\,\text{mg/m}^3$, respectively [51]. We can clearly observe from this figure that reducing the chlorophyll concentration level results in better BER performance. This phenomenon is attributed to the strong dependence of the absorption effect on chlorophyll concentration (C_c); the lower the value of C_c, the less attenuation occurs due to absorption. Similar to the analysis of outage probability, we observe the same floor effect at high SNR.

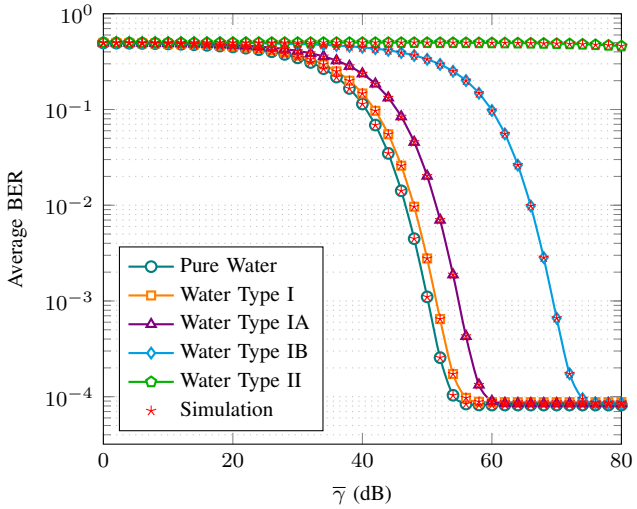

Fig. 6: Average BER for OOK using IM/DD technique for different Jerlov water types.

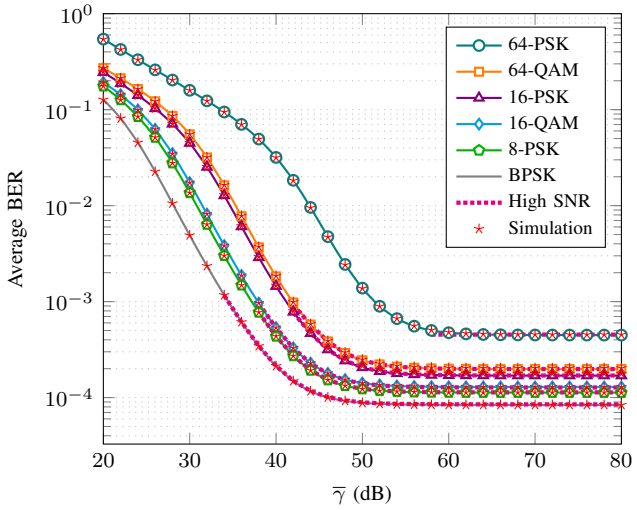

Fig. 7: Average BER for different modulation schemes using heterodyne detection technique for $\sigma_s = 3 \times r_a$.

The average BER performance for modulation schemes including 64-phase shift keying (PSK), 64-quadrature amplitude modulation (QAM), 16-PSK, 16-QAM, 8-PSK, and binary PSK, employing heterodyne detection technique is depicted in Fig. 7. As expected when the modulation order (M) exceeds 4,QAM outperforms M-PSK, and binary phase shift keying (BPSK) modulation provides the best performance when compared to the modulation schemes that have been presented. Furthermore, similar trends to those observed in the outage analysis, particularly regarding the BER floor and the tightness of the asymptotic expression obtained in (35) at high SNR, are noticeable in the figure.

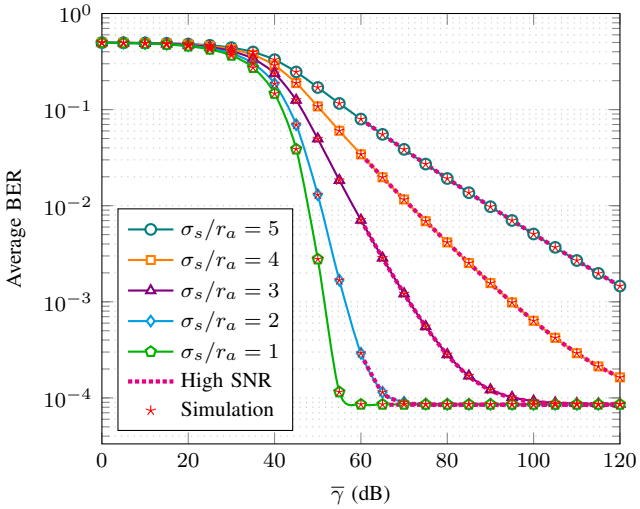

Fig. 8: Average BER for OOK using different values of the normalized beam deviation σ_s/r_a.

Fig. 8 presents the average BER for OOK using different normalized jitter values for the horizontal displacement σ_s/r_a along with the asymptotic results at high SNR. This figure clearly illustrates how the average BER deteriorates in the presence of severe pointing errors, as anticipated. As the value of the normalized jitter variance increases, the effect of pointing errors become more pronounced and worsens the BER performance.

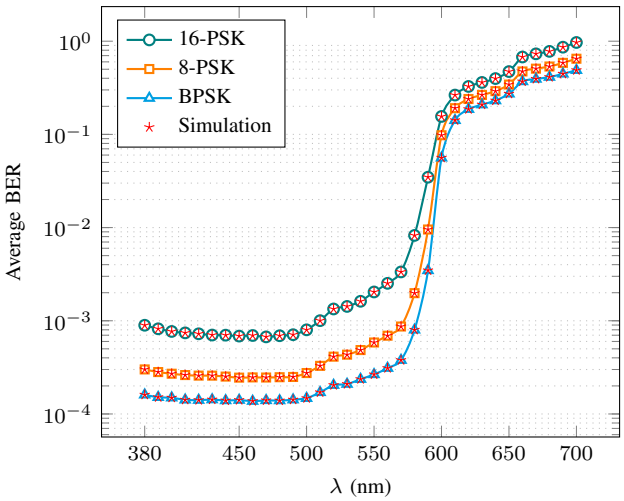

Fig. 9: Average BER using heterodyne detection versus the wavelength λ for BPSK, 8-PSK, and 16-PSK modulations with $\sigma_s = 3 \times r_a$ and $\overline{\gamma} = 40$ dB.

In Fig. 9, the average BER for 16-PSK, 8-PSK, and BPSK heterodyne modulation schemes is plotted versus the wavelength of the source, λ for pure water. As can be observed, the absorption effect significantly increases as the source wavelength increases, which results in a considerable reduction in the BER performance of the UOWC link. In addition, the strong dependence of the absorption effect on the source's

wavelength completely aligns with the experimental findings reported in [19]. More specifically, the absorption has the smallest effect on blue wavelengths and the highest effect on red wavelengths in the visible spectrum, as clearly shown in this figure.

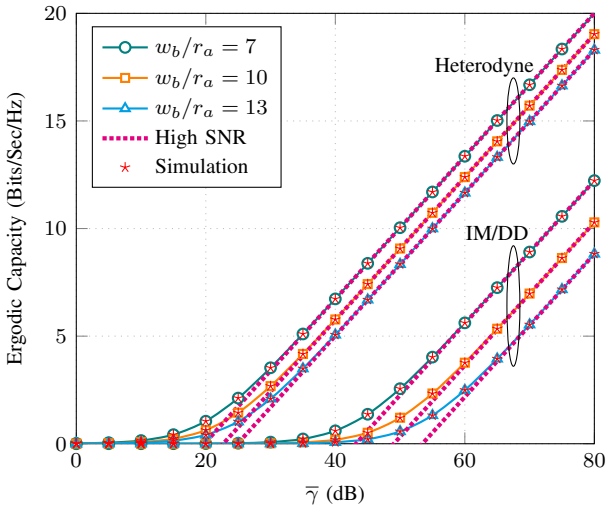

Fig. 10: Ergodic capacity for different values of the normalized beam waist w_b/r_a.

Fig. 10 presents the ergodic capacity performance under IM/DD and heterodyne detection schemes, considering different values of the normalized beam waist w_b/r_a. As clearly seen from this figure, utilizing a narrow beamwidth results in an improvement in the ergodic capacity performance due to the increased received signal power, regardless of the detection method employed at the receiver. Nevertheless, as mentioned in [52], a narrow beamwidth can make it simple for the transmitter to move from the line-of-sight (LoS) toward the receiver, which will accentuate the misalignment effect and cause a communication outage, under IM/DD or heterodyne methods. Fig. 10 also illustrates the asymptotic results of the ergodic capacity derived in (37) using the moments-based approach. As observed, there is a perfect match between the exact results and the high-SNR results, demonstrating the accuracy of the asymptotic analysis.

VII. Conclusion

The performance of an UOWC system that accounts for AOA fluctuations, pointing errors, attenuation, and turbulence has been examined in this paper in terms of the average BER, the outage probability, and the ergodic capacity when the optical link operates using either IM/DD or heterodyne techniques. Analytical and high SNR asymptotic formulas for these performance measures have been provided. The analytical and simulation results that have been presented clearly show how the UOWC system performance is affected by turbulence, attenuation, pointing errors, and AOA fluctuations. Results have demonstrated that increasing the receiver aperture diameter or the receiver FoV can lead to a significant improvement in performance of the UOWC link. Furthermore, pointing errors can severely impair performance, especially when the beam misalignment is asymmetrical. In addition, our results clearly demonstrated the detrimental impacts of the AOA fluctuations, particularly at high values of the beam deviation. It was also found that Jerlov water II, which has the highest concentration of chlorophyll, caused the greatest performance decline as a result of strong absorption effects. In all system settings, heterodyne method performs better than IM/DD, and coherent M-PSK modulation schemes outperform M-QAM modulation techniques.

Appendix A
Channel PDF Derivations

By inserting (7) and (17) into (16), we obtain

$$f_{h_{ag}|\theta_d}(h_{ag}) = \frac{\eta_s^2 a^a (b-1)^b}{2\pi q_H \mathrm{B}(a,b)} \int_{-\pi}^{\pi} \frac{h_{ag}^{\eta_s^2\xi(\varphi)-1}}{(A_0 h_{al}\cos\theta_d)^{\eta_s^2\xi(\varphi)}} \times \int_{\Delta_x}^{\infty} \frac{h_{at}^{a-\eta_s^2\xi(\varphi)-1}}{(a h_{at}+b-1)^{a+b}}\, dh_{at}\, d\varphi. \tag{A.1}$$

Utilizing [36, Eq. (3.194/2)], [53, Eq. (8.4.49.14)], and [36, Eq. (9.31.5)], (A.1) transforms to

$$f_{h_{ag}|\theta_d}(h_{ag}) = \frac{a\,\eta_s^2}{2\pi q_H (b-1) A_0 h_{al}\cos\theta_d \Gamma(a)\Gamma(b)} \times \int_{-\pi}^{\pi} \mathrm{G}_{2,2}^{2,1}\left[\frac{a h_{ag}}{(b-1)A_0 h_{al}\cos\theta_d}\middle| \begin{matrix} -b, \eta_s^2\xi(\varphi) \\ a-1, \eta_s^2\xi(\varphi)-1 \end{matrix}\right] d\varphi. \tag{A.2}$$

Now, the PDF of the channel can be determined by employing

$$f_h(h) = \int_0^{\theta_{FOV}} f_{h_{ag|\theta_d}}(h) f_{\theta_d}(\theta_d) d\theta_d + \delta(h) \int_{\theta_{FOV}}^{\infty} f_{\theta_d}(\theta_d) d\theta_d. \tag{A.3}$$

Substituting (15) and (A.2) into (A.3), we get

$$f_h(h) = \frac{a\,\eta_s^2}{2\pi q_H (b-1) A_0 h_{al}\Gamma(a)\Gamma(b)\sigma_0^2} \int_{-\pi}^{\pi}\int_0^{\theta_{FOV}} \frac{\theta_d \exp\left(-\frac{\theta_d^2}{2\sigma_0^2}\right)}{\cos\theta_d} \times \mathrm{G}_{2,2}^{2,1}\left[\frac{a h}{(b-1)A_0 h_{al}\cos\theta_d}\middle| \begin{matrix} -b, \eta_s^2\xi(\varphi) \\ a-1, \eta_s^2\xi(\varphi)-1 \end{matrix}\right] d\theta_d\, d\varphi + \delta(h) \int_{\theta_{FOV}}^{\infty} \frac{\theta_d}{\sigma_0^2} \exp\left(-\frac{\theta_d^2}{2\sigma_0^2}\right) d\theta_d. \tag{A.4}$$

Using the small angle approximation, i.e., $\cos\theta_d \approx 1$, and applying Eqs. (3.381/8) and (3.381/9) of [36], the PDF of the fading channel can be found as given in (18).

Appendix B
Channel CDF Derivations

Upon substituting the unified PDF of the SNR from (20) into (21), we have

$$F_\gamma(\gamma) = \frac{\eta_s^2\left[1-\exp\left(-\frac{\theta_{FOV}^2}{2\sigma_0^2}\right)\right]}{2\pi q_H r\Gamma(a)\Gamma(b)}\int_{-\pi}^{\pi}$$
$$\times\int_0^{\gamma} t^{-1}\mathrm{G}_{2,2}^{2,1}\left[\frac{a}{(b-1)A_0h_{al}}\left(\frac{t}{\overline{\gamma}}\right)^{\frac{1}{r}}\middle|\begin{matrix}1-b,1+\eta_s^2\xi(\varphi)\\ a,\eta_s^2\xi(\varphi)\end{matrix}\right]dtd\varphi$$
$$+\exp\left(-\frac{\theta_{FOV}^2}{2\sigma_0^2}\right)\frac{1}{r\overline{\gamma}^{\frac{1}{r}}}\int_0^{\gamma} t^{\frac{1}{r}-1}\delta\left(\left(\frac{t}{\overline{\gamma}}\right)^{\frac{1}{r}}\right)dt. \quad \text{(B.1)}$$

Changing variables as $x = (t/\overline{\gamma})^{1/r}$ for the last integral in (B.1) and then taking the integration accordingly will result in

$$F_\gamma(\gamma) = \frac{\eta_s^2\left[1-\exp\left(-\frac{\theta_{FOV}^2}{2\sigma_0^2}\right)\right]}{2\pi q_H r\Gamma(a)\Gamma(b)}\int_{-\pi}^{\pi}$$
$$\times\int_0^{\gamma} t^{-1}\mathrm{G}_{2,2}^{2,1}\left[\frac{a}{(b-1)A_0h_{al}}\left(\frac{t}{\overline{\gamma}}\right)^{\frac{1}{r}}\middle|\begin{matrix}1-b,1+\eta_s^2\xi(\varphi)\\ a,\eta_s^2\xi(\varphi)\end{matrix}\right]dtd\varphi$$
$$+\exp\left(-\frac{\theta_{FOV}^2}{2\sigma_0^2}\right)\mathrm{U}\left(\left(\frac{\gamma}{\overline{\gamma}}\right)^{\frac{1}{r}}\right), \quad \text{(B.2)}$$

where $\mathrm{U}(\cdot)$ represents the Heaviside step function. Now, to solve the t-dependent integral in (B.2), we perform a change of variables, setting $x = t^{1/r}$, and then apply [53, Eq. (2.24.1/2)] which leads to the CDF expression given in (28).

Appendix C
Moments Derivations

The moments can be obtained by inserting (20) into its definition $\mathbb{E}[\gamma^n] = \int_0^{\infty}\gamma^n f_\gamma(\gamma)\,d\gamma$. This substitution yields

$$\mathbb{E}[\gamma^n] = \frac{\eta_s^2\left[1-\exp\left(-\frac{\theta_{FOV}^2}{2\sigma_0^2}\right)\right]}{2r\pi q_H\Gamma(a)\Gamma(b)}\int_{-\pi}^{\pi}\int_0^{\infty}\gamma^{n-1}$$
$$\times\,\mathrm{G}_{2,2}^{2,1}\left[\frac{a}{(b-1)A_0h_{al}}\left(\frac{\gamma}{\overline{\gamma}}\right)^{\frac{1}{r}}\middle|\begin{matrix}1-b,1+\eta_s^2\xi(\varphi)\\ a,\eta_s^2\xi(\varphi)\end{matrix}\right]d\gamma\,d\varphi$$
$$+\frac{\exp\left(-\frac{\theta_{FOV}^2}{2\sigma_0^2}\right)}{r\overline{\gamma}^{\frac{1}{r}}}\int_0^{\infty}\gamma^{\frac{1}{r}+n-1}\delta\left[\left(\frac{\gamma}{\overline{\gamma}}\right)^{\frac{1}{r}}\right]d\gamma. \quad \text{(C.1)}$$

By employing the variable transformation $x = (\gamma/\overline{\gamma})^{1/r}$ and the property $\int_0^{\infty}\delta(x)f(x)dx = f(0)$, the second integral in (C.1) simplifies to 0. Through the change of variable $x = t^{1/r}$ and application of [53, Eq. (2.24.2/1)], the moments can be written as

$$\mathbb{E}[\gamma^n] = \int_{-\pi}^{\pi}\frac{\eta_s^2\,\Gamma(a+rn)\Gamma(b-rn)\left(1-\exp\left(-\frac{\theta_{FOV}^2}{2\sigma_0^2}\right)\right)}{2\pi q_H\Gamma(a)\Gamma(b)(\eta_s^2\xi(\varphi)+rn)}$$
$$\times\left[\frac{(b-1)A_0h_{al}\overline{\gamma}^{\frac{1}{r}}}{a}\right]^{rn}d\varphi. \quad \text{(C.2)}$$

By substituting (13) into (C.2) and performing some algebraic manipulations, we can easily derive the expression for the moments in (23).

Appendix D
Average BER Derivations

Inserting the unified PDF expression given in (20) into (25), we get

$$P_e = \frac{\delta\,\eta_s^2\left[1-\exp\left(-\frac{\theta_{FOV}^2}{2\sigma_0^2}\right)\right]}{4r\pi q_H\Gamma(a)\Gamma(b)\Gamma(p)}\int_{-\pi}^{\pi}\sum_{k=1}^{n_x}\int_0^{\infty}\frac{\Gamma(p,q_k\gamma)}{\gamma}$$
$$\times\,\mathrm{G}_{2,2}^{2,1}\left[\frac{a}{(b-1)A_0h_{al}}\left(\frac{\gamma}{\overline{\gamma}}\right)^{\frac{1}{r}}\middle|\begin{matrix}1-b,1+\eta_s^2\xi(\varphi)\\ a,\eta_s^2\xi(\varphi)\end{matrix}\right]d\gamma\,d\varphi$$
$$+\frac{\delta\exp\left(-\frac{\theta_{FOV}^2}{2\sigma_0^2}\right)}{2\Gamma(p)}\sum_{k=1}^{n_x}\int_0^{\infty}\frac{\Gamma(p,q_k\gamma)}{r\overline{\gamma}^{\frac{1}{r}}\gamma^{1-\frac{1}{r}}}\delta\left[\left(\frac{\gamma}{\overline{\gamma}}\right)^{\frac{1}{r}}\right]d\gamma. \quad \text{(D.1)}$$

For the last integral in (D.1), we first change variables as $t = (\gamma/\overline{\gamma})^{1/r}$ then we utilize the relationship $\int_0^{\infty}\delta(x)f(x)dx = f(0)$, resulting in

$$P_e = \frac{\delta\,\eta_s^2\left[1-\exp\left(-\frac{\theta_{FOV}^2}{2\sigma_0^2}\right)\right]}{4r\pi q_H\Gamma(a)\Gamma(b)\Gamma(p)}\int_{-\pi}^{\pi}\sum_{k=1}^{n_x}\int_0^{\infty}\frac{\Gamma(p,q_k\gamma)}{\gamma}$$
$$\times\,\mathrm{G}_{2,2}^{2,1}\left[\frac{a}{(b-1)A_0h_{al}}\left(\frac{\gamma}{\overline{\gamma}}\right)^{\frac{1}{r}}\middle|\begin{matrix}1-b,1+\eta_s^2\xi(\varphi)\\ a,\eta_s^2\xi(\varphi)\end{matrix}\right]d\gamma\,d\varphi$$
$$+\frac{n_x\delta}{2}\exp\left(-\frac{\theta_{FOV}^2}{2\sigma_0^2}\right). \quad \text{(D.2)}$$

To address the γ-dependent integral in (D.2), we express the incomplete upper Gamma function in terms of the MeijerG function according to [54, Eq. (06.06.26.0005.01)] then we utilize [53, Eq. (2.24.1/1)], yielding the unified average BER expression as given in (26).

Appendix E
Channel Capacity Derivations

Inserting the PDF of the SNR in (20) into (27), the equation of the ergodic capacity equation becomes

$$\overline{C} = \frac{\eta_s^2\left[1-\exp\left(-\frac{\theta_{FOV}^2}{2\sigma_0^2}\right)\right]}{2r\pi q_H\Gamma(a)\Gamma(b)}\int_{-\pi}^{\pi}\int_0^{\infty}\frac{\ln(1+c_r\gamma)}{\gamma}$$
$$\times\,\mathrm{G}_{2,2}^{2,1}\left[\frac{a}{(b-1)A_0h_{al}}\left(\frac{\gamma}{\overline{\gamma}}\right)^{\frac{1}{r}}\middle|\begin{matrix}1-b,1+\eta_s^2\xi(\varphi)\\ a,\eta_s^2\xi(\varphi)\end{matrix}\right]d\gamma\,d\varphi$$
$$+\frac{\exp\left(-\frac{\theta_{FOV}^2}{2\sigma_0^2}\right)}{r\overline{\gamma}^{\frac{1}{r}}}\int_0^{\infty}\gamma^{\frac{1}{r}-1}\ln(1+c_r\gamma)\delta\left[\left(\frac{\gamma}{\overline{\gamma}}\right)^{\frac{1}{r}}\right]d\gamma. \quad \text{(E.1)}$$

By employing the change of variable $t = (\gamma/\overline{\gamma})^{1/r}$, the second integral in (D.1) evaluates to 0. According to [55, Eq. (11)],

the logarithmic term in (E.1) can be represented with the relationship $\ln(1+x) = \mathrm{G}_{2,2}^{1,2}\left[x\middle|\begin{matrix}1,1\\1,0\end{matrix}\right]$, then, (E.1) becomes

$$\overline{C} = \frac{\eta_s^2\left[1-\exp\left(-\frac{\theta_{FOV}^2}{2\sigma_0^2}\right)\right]}{2r\pi q_H \Gamma(a)\Gamma(b)} \int_{-\pi}^{\pi}\int_{0}^{\infty} \gamma^{-1}\mathrm{G}_{2,2}^{1,2}\left[c_r\gamma\middle|\begin{matrix}1,1\\1,0\end{matrix}\right] \times \mathrm{G}_{2,2}^{2,1}\left[\frac{a}{(b-1)A_0 h_{al}}\left(\frac{\gamma}{\overline{\gamma}}\right)^{\frac{1}{r}}\middle|\begin{matrix}1-b, 1+\eta_s^2\xi(\varphi)\\ a, \eta_s^2\xi(\varphi)\end{matrix}\right] d\gamma\, d\varphi. \tag{E.2}$$

Finally, employing [53, Eq. (2.24.1/1)] and performing some algebraic manipulations, we arrive at the unified ergodic capacity equation for the underwater wireless optical channel, as presented in (28).

REFERENCES

[1] W. Jiang, B. Han, M. A. Habibi, and H. D. Schotten, "The road towards 6G: A comprehensive survey," *IEEE Open Journal of the Communications Society*, vol. 2, pp. 334–366, 2021.

[2] L. Nkenyereye, L. Nkenyereye, and B. Ndibanje, "Internet of underwater things: A survey on simulation tools and 5G-based underwater networks," *Electronics*, vol. 13, no. 3, 2024.

[3] R. Alghamdi, H. Dahrouj, T. Al-Naffouri, and M.-S. Alouini, "Toward immersive underwater cloud-enabled networks: Prospects and challenges," *IEEE BITS the Information Theory Magazine*, pp. 1–12, 2023.

[4] S. Li and L. Yang, "Analysis of a mixed multiuser underwater acoustic communication/free space optical heterogeneous relaying system," *IEEE Internet of Things Journal*, vol. 11, no. 11, pp. 20 718–20 730, 2024.

[5] H. M. Oubei, E. Zedini, R. T. ElAfandy, A. Kammoun, M. Abdallah, T. K. Ng, M. Hamdi, M.-S. Alouini, and B. S. Ooi, "Simple statistical channel model for weak temperature-induced turbulence in underwater wireless optical communication systems," *Optics Letters*, vol. 42, no. 13, pp. 2455–2458, 2017.

[6] N. Almaymoni, O. Alkhazragi, W. H. Gunawan, G. Melinte, T. K. Ng, and B. S. Ooi, "High-Speed 645-nm VCSELs for Low-Scattering-Loss Gb/s Underwater Wireless Optical Communications," *IEEE Photonics Technology Letters*, vol. 36, no. 6, pp. 377–380, 2024.

[7] Z. Zeng, S. Fu, H. Zhang, Y. Dong, and J. Cheng, "A survey of underwater optical wireless communications," *IEEE Communications Surveys Tutorials*, vol. 19, no. 1, pp. 204–238, 2017.

[8] P. Salcedo-Serrano, R. Boluda-Ruiz, J. M. Garrido-Balsells, and A. García-Zambrana, "On the scattering-induced fading for optical wireless links through seawater: statistical characterization and its applications," *Opt. Express*, vol. 29, no. 23, pp. 37 101–37 116, Nov. 2021.

[9] V. Guerra, J. Rufo, J. Rabadan, and R. Perez-Jimenez, "Effect of moving microalgae on underwater wireless optical links," *Appl. Opt.*, vol. 59, no. 2, pp. 515–520, Jan 2020.

[10] H. Safi, A. Dargahi, J. Cheng, and M. Safari, "Analytical channel model and link design optimization for ground-to-HAP free-space optical communications," *IEEE/OSA Journal of Lightwave Technology*, vol. 38, no. 18, pp. 5036–5047, 2020.

[11] H. Wen, H. Yin, X. Ji, and A. Huang, "Modeling and performance analysis of underwater wireless optical absorption, scattering, and turbulence channels employing Monte Carlo-multiple phase screens," *Appl. Opt.*, vol. 62, no. 26, pp. 6883–6891, Sep 2023.

[12] C. T. Geldard, J. S. Thompson, and W. O. Popoola, "On the relative effect of underwater optical turbulence in different channel conditions," *IEEE Access*, vol. 12, pp. 11 104–11 113, 2024.

[13] M. V. Jamali, A. Mirani, A. Parsay, B. Abolhassani, P. Nabavi, A. Chizari, P. Khorramshahi, S. Abdollahramezani, and J. A. Salehi, "Statistical studies of fading in underwater wireless optical channels in the presence of air bubble, temperature, and salinity random variations," *IEEE Transactions on Communications*, vol. 66, no. 10, pp. 4706–4723, 2018.

[14] E. Zedini, H. M. Oubei, A. Kammoun, M. Hamdi, B. S. Ooi, and M.-S. Alouini, "Unified statistical channel model for turbulence-induced fading in underwater wireless optical communication systems," *IEEE Transactions on Communications*, vol. 67, no. 4, pp. 2893–2907, 2019.

[15] Y. Baykal, Y. Ata, and M. C. Gökçe, "Underwater turbulence, its effects on optical wireless communication and imaging: A review," *Optics & Laser Technology*, vol. 156, p. 108624, 2022.

[16] L. Kou, J. Zhang, P. Zhang, Y. Yang, and F. He, "Composite channel modeling for underwater optical wireless communication and analysis of multiple scattering characteristics," *Opt. Express*, vol. 31, no. 7, pp. 11 320–11 334, Mar 2023.

[17] D. Chen, P. Zhao, L. Tang, and M. Wang, "Modeling and oblique transmission characteristics of an underwater wireless optical communication channel based on ocean depth layering," *J. Opt. Soc. Am. A*, vol. 41, no. 3, pp. 424–434, Mar 2024.

[18] V. I. Haltrin, "Chlorophyll-based model of seawater optical properties," *Applied Optics*, vol. 38, no. 33, pp. 6826–6832, 1999.

[19] A. Morel and L. Prieur, "Analysis of variations in ocean color 1," *Limnology and Oceanography*, vol. 22, no. 4, pp. 709–722, 1977.

[20] B. Cochenour, L. Mullen, and J. Muth, "Temporal response of the underwater optical channel for high-bandwidth wireless laser communications," *IEEE Journal of Oceanic Engineering*, vol. 38, no. 4, pp. 730–742, 2013.

[21] X. Wang, M. Zhang, H. Zhou, and X. Ren, "Performance analysis and design considerations of the shallow underwater optical wireless communication system with solar noises utilizing a photon tracing-based simulation platform," *Electronics*, vol. 10, no. 5, 2021.

[22] R. Cai, M. Zhang, D. Dai, Y. Shi, and S. Gao, "Analysis of the underwater wireless optical communication channel based on a comprehensive multiparameter model," *Applied Sciences*, vol. 11, no. 13, 2021.

[23] Y. Yang, F. He, Q. Guo, M. Wang, J. Zhang, and Z. Duan, "Analysis of underwater wireless optical communication system performance," *Appl. Opt.*, vol. 58, no. 36, pp. 9808–9814, Dec. 2019.

[24] M. Elamassie, F. Miramirkhani, and M. Uysal, "Performance characterization of underwater visible light communication," *IEEE Transactions on Communications*, vol. 67, no. 1, pp. 543–552, Jan. 2019.

[25] B. Majlesein, A. Gholami, and Z. Ghassemlooy, "Investigation of the scattering noise in underwater optical wireless communications," *Sci*, vol. 3, no. 2, 2021.

[26] Y. Li, Y. Zhang, and Y. Zhu, "Capacity of underwater wireless optical links with pointing errors," *Optics Communications*, vol. 446, pp. 16–22, 2019.

[27] J.-Y. Wang, P. Feng, L.-H. Hong, H.-N. Yang, and N. Liu, "Performance evaluation and optimization of UAV-based hybrid dual-hop FSO/UOWC systems," *IEEE Systems Journal*, vol. 70, pp. 1–12, 2024.

[28] R. Boluda-Ruiz, A. García-Zambrana, B. Castillo-Vázquez, and S. Hranilovic, "Impact of angular pointing error on BER performance of underwater optical wireless links," *Optics Express*, vol. 28, no. 23, pp. 34 606–34 622, 2020.

[29] R. Boluda-Ruiz, P. Salcedo-Serrano, B. Castillo-Vázquez, A. García-Zambrana, and J. M. Garrido-Balsells, "Impact of scattering on secrecy outage probability of underwater optical wireless links," *IEEE Journal of Oceanic Engineering*, vol. 48, no. 4, pp. 1362–1372, 2023.

[30] P. Salcedo-Serrano, R. Boluda-Ruiz, J. M. Garrido-Balsells, A. García-Zambrana, and S. Hranilovic, "Underwater optical wireless channel capacity under oceanic turbulence using spatial diversity techniques," in *ICC 2023-IEEE International Conference on Communications*. IEEE, 2023, pp. 1162–1168.

[31] H. Jiang, H. Qiu, N. He, W. Popoola, Z. Ahmad, and S. Rajbhandari, "Ergodic capacity and error performance of spatial diversity UWOC systems over generalized gamma turbulence channels," *Optics communications*, vol. 505, p. 127476, 2022.

[32] M. V. Jamali, P. Nabavi, and J. A. Salehi, "MIMO underwater visible light communications: Comprehensive channel study, performance analysis, and multiple-symbol detection," *IEEE Transactions on Vehicular Technology*, vol. 67, no. 9, pp. 8223–8237, 2018.

[33] W. Liu, Z. Xu, and L. Yang, "SIMO detection schemes for underwater optical wireless communication under turbulence," *Photonics Research*, vol. 3, no. 3, pp. 48–53, 2015.

[34] M. A. Chancey, *Short range underwater optical communication links*. North Carolina State University, 2005.

[35] K. P. Peppas, G. C. Alexandropoulos, E. D. Xenos, and A. Maras, "The Fischer–Snedecor $\mathcal{F}$-distribution model for turbulence-induced fading in free-space optical systems," *Journal of Lightwave Technology*, vol. 38, no. 6, pp. 1286–1295, 2020.

[36] I. S. Gradshteyn and I. M. Ryzhik, *Table of integrals, series, and products*. Academic press, 2014.

[37] L. C. Andrews and R. L. Phillips, "Laser beam propagation through random media," *Laser Beam Propagation Through Random Media: Second Edition*, 2005.

[38] M. Elamassie and M. Uysal, "Vertical underwater VLC links over cascaded Gamma-Gamma turbulence channels with pointing errors," in *2019 IEEE International Black Sea Conference on Communications and Networking (BlackSeaCom)*, 2019, pp. 1–5.
[39] G. Xu and J. Lai, "Average capacity analysis of the underwater optical plane wave over anisotropic moderate-to-strong oceanic turbulence channels with the Malaga fading model," *Opt. Express*, vol. 28, no. 16, pp. 24 056–24 068, Aug. 2020.
[40] Y. Ata, "Rytov variance of plane and spherical waves, and scintillation index in weak to strong underwater turbulence," *Journal of Optics*, vol. 24, p. 115601, 2022.
[41] Y. Ata and K. Kiasaleh, "Analysis of optical wireless communication links in turbulent underwater channels with wide range of water parameters," *IEEE Transactions on Vehicular Technology*, vol. 72, no. 5, pp. 6363–6374, 2023.
[42] M. Elamassie, M. Uysal, Y. Baykal, M. Abdallah, and K. Qaraqe, "Effect of eddy diffusivity ratio on underwater optical scintillation index," *JOSA*, vol. 34, no. 11, pp. 1969–1973, 2017.
[43] J.-R. Yao, M. Elamassie, and O. Korotkova, "Spatial power spectrum of natural water turbulence with any average temperature, salinity concentration, and light wavelength," *JOSA A*, vol. 37, no. 10, pp. 1614–1621, 2020.
[44] Y. Ata, J. Yao, and O. Korotkova, "BER variation of an optical wireless communication system in underwater turbulent medium with any temperature and salinity concentration," *Optics communications*, vol. 485, p. 126751, 2021.
[45] W. Gappmair, S. Hranilovic, and E. Leitgeb, "OOK performance for terrestrial FSO links in turbulent atmosphere with pointing errors modeled by Hoyt distributions," *IEEE Communications Letters*, vol. 15, no. 8, pp. 875–877, 2011.
[46] I. S. Ansari, F. Yilmaz, and M.-S. Alouini, "Performance analysis of free-space optical links over Malaga ($\mathcal{M}$) turbulence channels with pointing errors," *IEEE Transactions on Wireless Communications*, vol. 15, no. 1, pp. 91–102, 2015.
[47] C. A. Coelho and B. C. Arnold, *Finite form representations for Meijer G and Fox H functions*. Springer, 2019.
[48] A. A. Kilbas, *H-transforms: Theory and Applications*. CRC press, 2004.
[49] F. Yilmaz and M.-S. Alouini, "Novel asymptotic results on the high-order statistics of the channel capacity over generalized fading channels," in *IEEE 13th International Workshop on Signal Processing Advances in Wireless Communications (SPAWC'2012)*, 2012, pp. 389–393.
[50] J. Surof, J. Poliak, and R. M. Calvo, "Demonstration of intradyne BPSK optical free-space transmission in representative atmospheric turbulence conditions for geostationary uplink channel," *Opt. Lett.*, vol. 42, no. 11, pp. 2173–2176, Jun. 2017.
[51] Y. Ata and O. Korotkova, "Absorption, scattering, and optical turbulence in natural waters," *Appl. Opt.*, vol. 61, no. 15, pp. 4404–4411, May 2022.
[52] S. Arnon, "Optimization of urban optical wireless communication systems," *IEEE Transactions on Wireless Communications*, vol. 2, no. 4, pp. 626–629, 2003.
[53] A. Prudnikov, Y. Brychkov, and O. Marichev, *Integrals and Series, Volume 3: More Special Functions*. CRC, 1999.
[54] W. Inc., "The wolfram functions site." [Online]. Available: https://functions.wolfram.com
[55] V. Adamchik and O. Marichev, "The algorithm for calculating integrals of hypergeometric type functions and its realization in REDUCE system," in *Proceedings of the International Symposium on Symbolic and Algebraic Computation*, 1990, pp. 212–224.